

Perceptual-Distortion Balanced Image Super-Resolution is a Multi-Objective Optimization Problem

Qiwen Zhu

State Key Lab of MIPT, Huazhong
University of Science and Technology
Wuhan, China
zhuqiwen@hust.edu.cn

Yanjie Wang

School of AIA, Huazhong University
of Science and Technology
Wuhan, China
aiawyj@hust.edu.cn

Shilv Cai

School of AIA, Huazhong University
of Science and Technology
Wuhan, China
caishilv@hust.edu.cn

Liqun Chen

School of AIA, Huazhong University
of Science and Technology
Wuhan, China
chenliqun@hust.edu.cn

Jiahuan Zhou

Wangxuan Institute of Computer
Technology, Peking University
Beijing, China
jiahuanzhou@pku.edu.cn

Luxin Yan

State Key Lab of MIPT, Huazhong
University of Science and Technology
Wuhan, China
yanluxin@hust.edu.cn

Sheng Zhong

State Key Lab of MIPT, Huazhong
University of Science and Technology
Wuhan, China
zhongsheng@hust.edu.cn

Xu Zou*

State Key Lab of MIPT, Huazhong
University of Science and Technology
Wuhan, China
zoux@hust.edu.cn

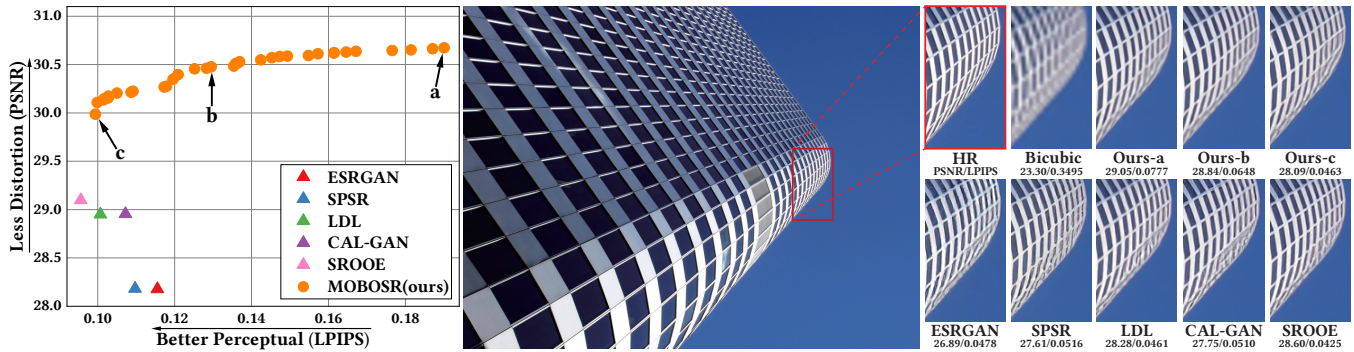


Figure 1: Left: Comparisons on the DIV2K [1] validation set, our method not only significantly surpasses others in distortion metrics (PSNR) but also holds an advantage in perceptual quality (LPIPS [58]). [a, b, c] represent three different sample points on the perception-distortion Pareto frontier to illustrate the trade-off between distortion and perceptual quality. Right: From the quantitative and visual comparison of this single image, it is evident from our results, labeled as Ours-[a, b, c], that as PSNR decreases and LPIPS increases along the Pareto frontier, the images become sharper. However, this sharpness is accompanied by the introduction of noise and artifacts. In contrast to other methods, our method generates fewer artifacts and avoids excessive blurring, which can be attributed to our model achieving an optimal balance between perceptual quality and distortion.

*Corresponding author.

Permission to make digital or hard copies of all or part of this work for personal or classroom use is granted without fee provided that copies are not made or distributed for profit or commercial advantage and that copies bear this notice and the full citation on the first page. Copyrights for components of this work owned by others than the author(s) must be honored. Abstracting with credit is permitted. To copy otherwise, or republish, to post on servers or to redistribute to lists, requires prior specific permission and/or a fee. Request permissions from permissions@acm.org.

MM '24, October 28–November 1, 2024, Melbourne, VIC, Australia

© 2024 Copyright held by the owner/author(s). Publication rights licensed to ACM.

ACM ISBN 979-8-4007-0686-8/24/10

<https://doi.org/10.1145/3664647.3681512>

Abstract

Training Single-Image Super-Resolution (SISR) models using pixel-based regression losses can achieve high distortion metrics scores (e.g., PSNR and SSIM), but often results in blurry images due to insufficient recovery of high-frequency details. Conversely, using GAN or perceptual losses can produce sharp images with high perceptual metric scores (e.g., LPIPS), but may introduce artifacts and incorrect textures. Balancing these two types of losses can help achieve a trade-off between distortion and perception, but the challenge lies in tuning the loss function weights. To address this issue, we propose a novel method that incorporates Multi-Objective Optimization (MOO) into the training process of SISR models to

balance perceptual quality and distortion. We conceptualize the relationship between loss weights and image quality assessment (IQA) metrics as black-box objective functions to be optimized within our Multi-Objective Bayesian Optimization Super-Resolution (MOBOSR) framework. This approach automates the hyperparameter tuning process, reduces overall computational cost, and enables the use of numerous loss functions simultaneously. Extensive experiments demonstrate that MOBOSR outperforms state-of-the-art methods in terms of both perceptual quality and distortion, significantly advancing the perception-distortion Pareto frontier. Our work points towards a new direction for future research on balancing perceptual quality and fidelity in nearly all image restoration tasks. The source code and pretrained models are available at: <https://github.com/ZhuKeven/MOBOSR>.

CCS Concepts

• **Computing methodologies** → **Reconstruction**.

Keywords

Super Resolution, Perceptual Quality, Distortion, Multi-Objective Optimization, Loss Function

ACM Reference Format:

Qiwen Zhu, Yanjie Wang, Shilv Cai, Liqun Chen, Jiahuan Zhou, Luxin Yan, Sheng Zhong, and Xu Zou. 2024. Perceptual-Distortion Balanced Image Super-Resolution is a Multi-Objective Optimization Problem. In *Proceedings of the 32nd ACM International Conference on Multimedia (MM '24)*, October 28–November 1, 2024, Melbourne, VIC, Australia. ACM, New York, NY, USA, 10 pages. <https://doi.org/10.1145/3664647.3681512>

1 Introduction

Super-resolution (SR) plays a crucial role in multimedia, increasingly integrated into devices to enhance the viewing experience of low-resolution images and videos, not only improve visual quality but also reducing bandwidth and storage needs for media streaming.

In the single-image super-resolution (SISR) field, both model architecture and computational efficiency have received considerable attention, resulting in impressive achievements. The majority of these studies report and compare results using PSNR and SSIM [55], both of which are pixel-based metrics. Thus, SR task is actually treated as a regression problem, using regression losses to train, such as L1 Normalization (Mean Absolute Error), L2 Normalization (Mean Squared Error), Charbonnier loss [22], and Huber loss [23]. Pixel-based regression losses are favored for their simplicity and computational efficiency. However, as image downscaling results in significant loss of high-frequency details, SR poses an ill-posed problem. Pixel-based regression loss functions struggle with recovering these high-frequency details [26, 40], often producing blurred images, despite achieving high PSNR and SSIM [55] scores.

While PSNR or SSIM [55] are convenient for computation and comparison, they do not adequately reflect the perceptual quality of images and may even have a negative correlation with human perception (see Figure 1, ‘Ours-a’ has higher PSNR than ‘Ours-c’ while ‘Ours-a’ is more blurry on the contrary). The most accurate reflection of human perceptual quality is naturally human-opinion-scores (HOS), but due to its irreproducibility and high cost, it is challenging to use for fair comparative analysis [4]. Consequently,

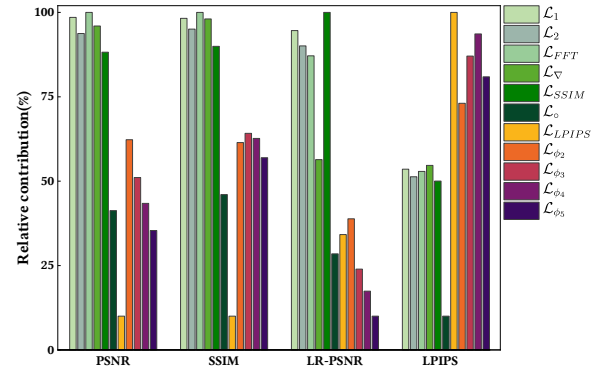


Figure 2: Relative contributions of each loss function to the final model metrics. The definitions of these loss functions are detailed in Section 4.1. The relative contribution are calculated by training a SR model with each individual loss function and evaluating them on the DIV2K [1] validation set. Metrics are normalized, so a higher bar indicates better performance for the corresponding metric. This indicates there is an inherent conflict between perceptual and regression losses (e.g. $[\mathcal{L}_1, \mathcal{L}_2, \mathcal{L}_{FFT}, \mathcal{L}_\nabla, \mathcal{L}_{SSIM}]$ contribute more to distortion metrics (PSNR, SSIM [55], and LR-PSNR), while $[\mathcal{L}_{LPIPS}, \mathcal{L}_{\phi_2}, \mathcal{L}_{\phi_3}, \mathcal{L}_{\phi_4}, \mathcal{L}_{\phi_5}]$ contribute more to perceptual metric (LPIPS [58])).

Full Reference Image Quality Assessment (FR-IQA) metrics like LPIPS [58] have been developed to better align with human perception while being reproducible and computationally efficient. And to enhance the perceptual quality of SR models, researchers commonly employ perceptual loss [19] or GAN [16] for training, which, while enhancing image sharpness, may also result in the introduction of noise and artifacts (see Figure 1, ‘SPSR’ [31] holds better LPIPS [58] than ‘Ours-b’, but ‘SPSR’ [31] causes much more artifacts).

Therefore, many researchers combine regression and perceptual losses to strive for an optimal balance between pixel accuracy and visual perception [10, 14, 15, 26, 28, 37, 40, 47, 50, 53]. However, as shown in Figure 2, there is an inherent conflict between perceptual loss [19] and regression losses, as well as between perceptual and distortion metrics [5], leading to a compromise.

Several methods attempt to balance perception and distortion by manually setting the weights of different losses during training [15, 24, 38, 41, 53]. Concurrently, some approaches involve training two structurally identical networks: one employs regression loss to optimize distortion metrics, while the other adopts perceptual loss [19] to enhance perceptual metrics. The parameters of these networks are subsequently blended through interpolation, employing manually determined weights to finely adjust the trade-off between perception and distortion within the final model [47, 52, 53]. In a novel strategy, Wang et al. [50] incorporated conditional branches into the network, which are regulated by a scalar value to produce varying trade-offs. Furthermore, certain methods selectively apply different losses to different regions or frequency components of an image [10, 14, 26, 28, 37, 40, 51]. This entails utilizing perceptual loss [19] or GAN [16] for areas with intricate textures to

maximize perceptual quality, while reserving pixel regression loss for regions with simpler textures to maintain fidelity. While these artworks have garnered notable success, they have not yet explored the optimal balance boundary between perception and distortion. Furthermore, they either require laborious hyperparameter tuning or impose additional computational demands during the inference phase, and can only apply a limited number of loss functions.

To intuitively illustrate the conflict between perception and distortion, we conducted a series of simple experiments to quantify the contributions of various loss functions to different IQA metrics, as depicted in Figure 2. It was observed that loss functions with a higher contribution to distortion metrics inversely contributed less to perceptual metrics, and vice versa. This conflicting characteristic prompted us to consider: **Whether Multi-Objective Optimization (MOO) could be a viable solution to this dilemma?**

MOO is an optimization strategy designed to simultaneously address multiple objectives. Due to potential contradictions among these objectives, it is often challenging to find a single solution that maximizes or minimizes all objectives concurrently. Therefore, the aim of MOO is to identify a set of solutions that offer the best compromise among the different objectives, culminating in what is known as the Pareto frontier. On this frontier, any improvement in one objective comes at the cost of compromising at least one other objective. Multi-Objective Bayesian Optimization (MOBO), a widely utilized algorithm within the MOO framework, is particularly adept at optimizing black-box objective functions that are gradient-inaccessible and costly to evaluate.

This paper introduces a novel application of MOBO to address the challenge of balancing perceptual quality and distortion in SISR models. We conceptualize the relationship between loss weights and IQA metrics as black-box objective functions to be optimized. In the training process, the performance metrics of SR models guide the optimization algorithm to refine the loss weights for the next epoch, thereby creating a feedback loop that enhances model efficacy with each iteration. This approach avoids the typical computational overhead associated with AutoML, where each optimization iteration requires a complete model retraining. It incurs no additional computational or storage costs during inference and can apply numerous loss functions during training.

In summary, the contributions of this work are threefold:

- We pioneer the application of MOBO to address the challenge of balancing perception quality and distortion in SISR models.
- We have developed a method for dynamically adjusting loss weights during model training, thereby obviating the need for hyperparameter tuning and significantly reducing the computational resources required in comparison to AutoML hyperparameter search methods.
- This research expands the perceptual-distortion Pareto frontier of the SISR domain, offering new insights into the trade-offs between perceptual quality and distortion in various image restoration tasks.

2 Related Works

Our work employs MOBO to address the balance between perception and distortion in SISR models. The following sections will

provide an overview of SISR methods aimed at addressing this balance, followed by a concise introduction to MOO methods.

2.1 Single Image Super Resolution

Since Dong et al. [11] first applied CNN to the task of SISR, this field has been predominantly driven by deep learning advancements. SISR models have continuously improved in performance. Notably, ESPCN [42] has replaced interpolation with sub-pixel convolution and deferred scaling to the end of the model, significantly reducing computational demands. EDSR [27] has achieved enhanced performance by omitting Batch Normalization [18] layers, which, despite their effectiveness in other tasks, proved detrimental to SR tasks. Furthermore, SwinIR [25] has constructed SR models based on Swin Transformer [29], establishing a new SOTA. These methods employ regression loss for training, achieving high PSNR and SSIM [55] scores but failing to recover high-frequency details, resulting in blurred images.

Johnson et al. [19] introduced perceptual loss which utilizes feature maps extracted from a pre-trained deep convolutional network (such as VGG [43]) as the input for the loss function, significantly enhancing the perceptual quality of super-resolution models. SR-GAN [24] pioneered the application of GAN [16] to SR models, enabling the generation of sharp details. These two seminal works have inspired a plethora of perception-oriented SR approaches. Beyond perceptual [19] and GAN [16] losses, a plethora of other loss functions have been incorporated into SISR models. A category of these introduces additional constraints, including: frequency domain constraints [6, 10, 15, 28, 44, 49], which utilize the spectral maps generated by FFT, DCT or Wavelet transformations to compute loss; gradient constraints [6, 30, 31, 46, 47, 54], which calculate loss using the gradient maps of images; and low-resolution consistency constraints [34, 46], which compute loss by comparing the downsampled super-resolved images with the original low-resolution images, thereby reducing the likelihood of generating incorrect textures. The application of these losses can further enhance certain metrics of SISR models, as shown in Figure 2.

2.2 Perceptual Distortion Trade-Off

However, while perceptual loss [19] and GAN [16] can enhance perceptual quality, they also introduce noise or artifacts and may even produce incorrect textures. To balance perceptual quality and distortion in SISR, most methods involve manually adjust the weights of different loss functions [15, 24, 38, 41, 53], necessitating extensive hyperparameter tuning to achieve superior outcomes, yet without guaranteeing optimality. Vu et al. [47], along with Wang et al. [52, 53], have demonstrated that a balance between perception quality and distortion can be attained through network parameter interpolation. This method mitigates the need for extensive network training for each weight by limiting the process to just two networks, thereby substantially reducing resource consumption. However, it is important to note that this approach still does not guarantee optimal results. In a similar way, Wang et al. [50] introduced conditional branches within the network architecture, modulated by a scalar parameter, to facilitate a spectrum of trade-offs. However, this approach introduces additional computational load during inference phase.

Rad et al. [40] categorized images into background, edges, and objects, applying different loss functions to each category. Fritsche et al. [14] employed separate loss functions for the high-frequency and low-frequency components of images. Liang et al. [26] divided images into numerous patches, classifying them into three categories—solid colors, texture-rich like trees or hair, and those with strong edge transitions—and applied different loss functions accordingly. Liu et al. [28] segmented images based on Spectral Bayesian Uncertainty before applying various loss functions. Park et al. [37] train an auxiliary network using the LPIPS [58] Map as supervisory signal to predict a discrete set of predefined loss weight combinations, aiming to maximum perceptual quality. These methods either fail to achieve the optimal balance, necessitate additional network training, or increase computational load during inference. Decomposing images before super-resolution and then recombining them may also potentially introduce more noise or artifacts.

2.3 Multi-Objective Optimization

MOO is a process that seeks to find the optimal balance among several often conflicting objectives. If the user has a clear preference for each objective, a weighted sum approach can be employed to transform it into a single-objective optimization problem. Conversely, if the user’s preferences are not well-defined, MOO techniques are necessary to determine the Pareto frontier.

In the field of MOO, the two main methodologies are multi-objective evolutionary algorithms (MOEA) and multi-objective Bayesian optimization (MOBO). MOEAs, such as NSGA-II [9], SPEA2 [59], MOEA/D [57], SMPSO [35] etc., are well-regarded for their ability to generate a diverse set of Pareto-optimal solutions through population-based approaches. They excel in exploring the solution space, which is crucial for capturing the trade-offs among conflicting objectives. However, MOEAs can be computationally demanding, especially when scaling to problems with high-dimensional objective spaces or when requiring a high-resolution Pareto front.

MOBO approaches extends Bayesian Global Optimization (BGO) [20] from single-objective to multi-objective contexts. It typically uses Gaussian Processes (GP) for modeling the objective functions and utilizes heuristic acquisition functions, such as Expected Hypervolume Improvement (EHVI) [7, 8, 13, 48], to identify the subsequent data point for evaluation. MOBO is highly sample efficient and is particularly well-suited for optimizing black-box objective functions which are expensive to evaluate. Thus, MOBO is especially well-suited for implementing our proposed SISR approach that balances perceptual quality and distortion.

3 Method

3.1 Preliminary

MOO refers to simultaneously optimizing multiple objective functions $f(x) \subset \mathbb{R}^M$ over a bounded search space $\mathcal{X} \in \mathbb{R}^d$, aiming to find solutions that optimize all objectives. However, these objectives often conflict with each other, making it challenging to find a single solution that optimizes all objectives simultaneously. Instead, we typically obtain a compromise among multiple objectives. A common approach is to identify the **Pareto front**.

Definition 1: Given $f(x) = [f_1(x), \dots, f_M(x)]$ and $f(x') = [f_1(x'), \dots, f_M(x')]$, if $f_i(x) \geq f_i(x')$ for all $i = 1, \dots, M$,

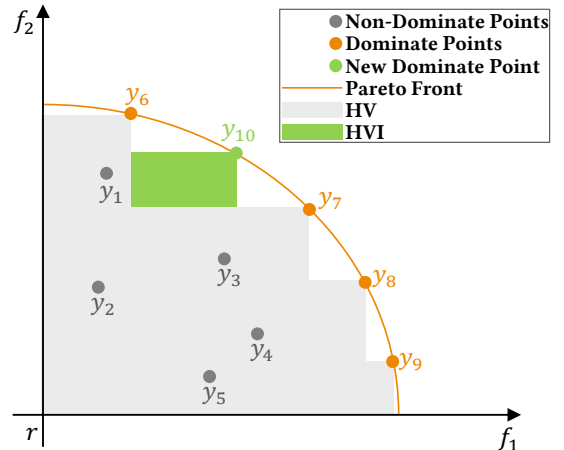


Figure 3: A toy example that demonstrates the 2-dimensional Pareto frontier, along with the HV and HVI.

and there exists at least one $i \in 1, \dots, M$ such that $f_i(x) > f_i(x')$, we say that $f(x)$ **dominates** $f(x')$, denoted as $f(x) > f(x')$.

Definition 2: An $f(x^*)$ is considered **Pareto optimal** if no other solution can dominate it.

Definition 3: In the space of objective functions, the set of all Pareto optimal solutions forms the **Pareto front**: $\mathcal{P} = \{f(x) \text{ s.t. } \nexists x' \in \mathcal{X} : f(x') > f(x)\}$.

Definition 4: **Hypervolume (HV)** quantifies the volume of the space dominated by a finite approximate Pareto front \mathcal{P} , with respect to a reference point $r \in \mathbb{R}^M$. Specifically, it measures the M -dimensional Lebesgue measure λ_M of the region that is bounded by the hyper-rectangle formed by vertices r and y_i : $HV(\mathcal{P}, r) = \lambda_M(\cup_{i=1}^{|\mathcal{P}|} [r, y_i])$.

Definition 5: **Hypervolume Improvement (HVI)** assesses the improvement achieved by a set of points \mathcal{Y} concerning a given Pareto front \mathcal{P} , relative to a reference point r : $HVI(\mathcal{Y}, \mathcal{P}, r) = HV(\mathcal{P} \cup \mathcal{Y}, r) - HV(\mathcal{P}, r)$.

Figure 3 presents an intuitive 2-dimensional toy example of these definitions. When optimizing an objective function $f(x)$ that is expensive to evaluate and lacks gradient information, MOBO emerges as the most suitable approach. It constructs a probabilistic surrogate model representing the objective function and employs an acquisition function to determine the next sampling point. Through iterative updates of the surrogate model, MOBO can efficiently identify the global optimum with fewer evaluations.

3.2 Problem Formulation

The primary goal of SISR is to employ a model, *e.g.* a neural network, denoted as G_θ and parameterized by θ , to transform a low-resolution input image I^{LR} , which is typically obtained through bicubic downsampling from a high-resolution image I^{HR} , into a super-resolved image I^{SR} with the same resolution as I^{HR} :

$$I^{SR} = G_\theta(I^{LR}). \quad (1)$$

The goal is to make I^{SR} as close as possible to I^{HR} , and to achieve this, we minimize a loss function:

$$\arg \min_{\theta} \mathcal{L}(G_{\theta}(I^{LR}), I^{HR}). \quad (2)$$

However, relying solely on a single loss function may not lead to an optimal model, as different loss functions have different advantages and drawbacks. Therefore, we linearly combine multiple losses:

$$\mathcal{L} = \sum_{i=1}^N \omega_i \mathcal{L}_i. \quad (3)$$

The gradient of this combined loss with respect to θ is:

$$\frac{\partial \mathcal{L}}{\partial \theta} = \sum_{i=1}^N \omega_i \frac{\partial \mathcal{L}_i}{\partial \theta}. \quad (4)$$

Therefore, by adjusting the weights ω_i of each loss \mathcal{L}_i , we can control the corresponding magnitude of the loss gradient and, consequently, its impact on the IQA metrics $\mathbf{Q}_{\theta} = [PSNR_{\theta}, \dots, LPIPS_{\theta}]$ of SR model. There exists a deterministic relationship between \mathbf{Q}_{θ} and loss weights $\boldsymbol{\omega} = [\omega_1, \dots, \omega_N]$:

$$\mathbf{Q}_{\theta} = f(\boldsymbol{\omega}). \quad (5)$$

Solving for f allows us to achieve optimal balance between perceptual quality and distortion by setting the best loss weights. However, since f is an unknown black-box function and these objectives may conflict with each other, MOBO will be employed for its estimation.

3.3 Multi-Objective Bayesian Optimization Super-Resolution

Initially, we randomly and uniformly sample a certain number of initial weights within the search space $\boldsymbol{\omega} \in \Omega^d$, train the SR model using the sampled weights, and then compute the IQA metrics of the SR model to obtain the observed dataset $\mathcal{D} = \{(\mathbf{Q}_i, \boldsymbol{\omega}_i)\}_{i=1}^T$.

Subsequently, we use the observed data \mathcal{D} to fit a probabilistic surrogate model. Surrogate models typically employ Gaussian processes (GP), which simulates the probability distribution of the true objective function f based on the observed data \mathcal{D} :

$$f \sim \mathcal{GP}(\boldsymbol{\mu}, \mathbf{K}), \quad (6)$$

where $\boldsymbol{\mu}$ is the mean function, and \mathbf{K} is the covariance function. In MOBO, a GP is fitted for each objective.

Given the high cost of evaluating the objective function and the low cost of evaluating the surrogate model, BO utilizes acquisition functions to heuristically select the next data point for evaluating and training, thereby minimizing the number of evaluations. Acquisition functions assess the potential performance of new data point based on the distribution predicted by the surrogate model. The most commonly used acquisition function is the Expected Improvement (EI):

$$\alpha_{EI}(\boldsymbol{\omega}) = \mathbb{E}[\max(0, f(\boldsymbol{\omega}^*) - f(\boldsymbol{\omega}))], \quad (7)$$

which can achieves a good balance between exploration and exploitation. When extended to multi-objective scenarios, the Expected Hypervolume Improvement (EHVI) is used as the acquisition function:

$$\alpha_{EHVI}(\boldsymbol{\omega}|\mathcal{P}) = \mathbb{E}[HVI(f(\boldsymbol{\omega})|\mathcal{P})]. \quad (8)$$

Algorithm 1: MOBOSR Pseudocode

Data: Pretrain epochs T_{init} , total epochs T , $i \leftarrow 1$.
Result: SR models $\mathcal{M} = \{M_1, \dots, M_N\}$ on optimal distortion and perceptual Pareto frontier.

- 1 Define optimization objectives \mathbf{Q} , parameters $\boldsymbol{\omega}$, dataset \mathcal{D} , objective function $f \sim \mathcal{GP}(\boldsymbol{\mu}, \mathbf{K})$, acquisition function $\alpha_{EHVI}(\boldsymbol{\omega}|\mathcal{P})$, SR model M ;
- 2 **for** $i = 1$ to T_{init} **do**
- 3 Random sample $\boldsymbol{\omega}_i \in \Omega^d$;
- 4 $M.train(\boldsymbol{\omega}_i)$;
- 5 $\mathbf{Q}_i = M.eval()$;
- 6 $\mathcal{D} = \mathcal{D} \cup \{(\mathbf{Q}_i, \boldsymbol{\omega}_i)\}$;
- 7 **end**
- 8 **for** $i = 1$ to T **do**
- 9 Fit $f \sim \mathcal{GP}(\boldsymbol{\mu}, \mathbf{K})$ using \mathcal{D} ;
- 10 $\boldsymbol{\omega}_i = \arg \max_{\boldsymbol{\omega} \in \Omega^d} \alpha_{EHVI}(\boldsymbol{\omega}|\mathcal{P})$;
- 11 $M.train(\boldsymbol{\omega}_i)$;
- 12 $\mathbf{Q}_i = M.eval()$;
- 13 $\mathcal{D} = \mathcal{D} \cup \{(\mathbf{Q}_i, \boldsymbol{\omega}_i)\}$;
- 14 **end**
- 15 Obtain \mathcal{M} through compute Pareto frontier from \mathcal{D} .

Through the acquisition function, we iteratively select the next most valuable point for evaluation and update the surrogate model:

$$\boldsymbol{\omega}^* = \arg \max_{\boldsymbol{\omega} \in \Omega^d} \alpha(\boldsymbol{\omega}). \quad (9)$$

By repeating these steps, BO can achieve the global optimum of the black-box objective function with a minimal number of evaluation steps. The pseudocode for the overall optimization process is outlined as Algorithm 1.

4 Experiments

4.1 Implementation Details

Model Architecture. The ESRGAN [53] architecture was employed as the SR model to evaluate the approach, due to its excellent performance and popularity in recent perception-related SR research. The widespread adoption of ESRGAN [53] and its proposed RRDB [53] backbone ensures a comprehensive and equitable comparison of our methodology.

Loss Functions. The loss functions we employed include:

- L1 Loss:

$$\mathcal{L}_1 = \left\| I^{SR} - I^{HR} \right\|_1. \quad (10)$$

- L2 Loss:

$$\mathcal{L}_2 = \left\| I^{SR} - I^{HR} \right\|_2^2. \quad (11)$$

- FFT Loss:

$$\mathcal{L}_{FFT} = \left\| FFT(I^{SR}) - FFT(I^{HR}) \right\|_1. \quad (12)$$

- Gradient Loss:

$$\mathcal{L}_{\nabla} = \left\| \nabla_h I^{SR} - \nabla_h I^{HR} \right\|_1 + \left\| \nabla_v I^{SR} - \nabla_v I^{HR} \right\|_1, \quad (13)$$

Table 1: Comparison of MOBOSR with other artworks on 7 datasets. The best and second-best results are highlighted in bold and underline, respectively. The symbols \uparrow and \downarrow indicate that higher or lower values of the metric are preferable. To the best of our knowledge, for fair comparisons, all publicly available methods (utilize RRDB [53] as the backbone, and aim to address the balance between perceptual quality and distortion) are selected. This includes SPSR [31], RRDB+LDL [26], CAL-GAN [36] and SROOE [37]. In this table, we use the data point labeled as Our-c in Figure 1 for comparison. Except for SROOE [37], our proposed MOBOSR consistently outperforms existing methods by a large margin on all metrics, particularly demonstrating a significant advantage in LR-PSNR with over 5dB improvements. Compared to SROOE [37], we achieve superior performance on all distortion metrics with similar LPIPS [58], even though we only train on the smaller DIV2K [1] training set. Quantitative comparisons of Ours-[a,b] and details on metric evaluation are available in the supplementary material.

Metrics	Methods	Train Datasets	Set5	Set14	DIV2K	BSD100	Urban100	General100	Manga109
PSNR \uparrow	ESRGAN [53]	DF2K-OST	30.4618	26.2839	28.1778	25.2892	24.3617	29.4593	28.5041
	SPSR [31]	DIV2K	30.3871	26.6501	28.1824	25.4949	24.8063	29.4794	28.6102
	RRDB+LDL [26]	DIV2K	31.0007	27.2064	28.9510	26.0988	25.4781	30.1974	29.4111
	CAL-GAN [36]	DIV2K	31.0475	<u>27.3272</u>	28.9549	<u>26.2581</u>	25.2908	30.0742	29.1665
	SROOE [37]	DF2K	<u>31.2455</u>	27.2561	29.0990	26.1715	<u>25.8452</u>	<u>30.4723</u>	<u>29.9017</u>
	Ours-c	DIV2K	31.8272	28.1766	29.9858	27.0494	26.0764	31.1164	30.2763
SSIM \uparrow	ESRGAN [53]	DF2K-OST	0.8518	0.6982	0.7761	0.6496	0.7341	0.8102	0.8604
	SPSR [31]	DIV2K	0.8432	0.7133	0.7720	0.6571	0.7472	0.8095	0.8591
	RRDB+LDL [26]	DIV2K	0.8610	0.7343	0.7952	0.6811	0.7670	0.8278	0.8746
	CAL-GAN [36]	DIV2K	0.8552	<u>0.7353</u>	0.7897	0.6789	0.7623	0.8262	0.8676
	SROOE [37]	DF2K	<u>0.8651</u>	0.7304	<u>0.7980</u>	<u>0.6866</u>	<u>0.7764</u>	<u>0.8332</u>	<u>0.8786</u>
	Ours-c	DIV2K	0.8804	0.7615	0.8203	0.7109	0.7812	0.8495	0.8938
LR-PSNR \uparrow	ESRGAN [53]	DF2K-OST	46.7348	43.8433	45.9012	43.8190	42.9339	45.4220	43.9667
	SPSR [31]	DIV2K	46.3607	43.6201	44.8529	42.6756	42.6679	44.6786	44.3872
	RRDB+LDL [26]	DIV2K	48.5067	46.2893	47.9757	45.1571	46.5827	48.0079	47.8923
	CAL-GAN [36]	DIV2K	42.4327	41.5963	42.8611	41.0666	41.6069	43.4227	42.8636
	SROOE [37]	DF2K	<u>53.1781</u>	<u>51.0679</u>	<u>53.5488</u>	<u>51.2347</u>	<u>50.6700</u>	<u>52.9797</u>	<u>51.7820</u>
	Ours-c	DIV2K	54.3372	53.3344	55.2161	53.3618	52.9401	54.5283	53.4195
LPIPS \downarrow	ESRGAN [53]	DF2K-OST	0.0750	0.1341	0.1155	0.1617	0.1228	0.0876	0.0647
	SPSR [31]	DIV2K	0.0616	0.1313	0.1097	0.1629	0.1186	0.0866	0.0662
	RRDB+LDL [26]	DIV2K	0.0637	0.1309	0.1007	0.1635	<u>0.1097</u>	0.0794	<u>0.0546</u>
	CAL-GAN [36]	DIV2K	0.0687	0.1320	0.1072	0.1696	0.1171	0.0894	0.0688
	SROOE [37]	DF2K	0.0603	0.1131	0.0956	<u>0.1514</u>	0.1067	0.0758	0.0511
	Ours-c	DIV2K	<u>0.0607</u>	<u>0.1240</u>	<u>0.0994</u>	0.1508	0.1154	<u>0.0776</u>	0.0576

where ∇_h and ∇_v are the Sobel gradient operators in the horizontal and vertical directions.

- Perceptual Loss [19]:

$$\mathcal{L}_{\phi_j} = \left\| \phi_j(I^{SR}) - \phi_j(I^{HR}) \right\|_1, j \in \{2, 3, 4, 5\}, \quad (14)$$

where ϕ_j is the feature map output by the VGG [43] network's j th layer.

- Cycle Consistency Loss:

$$\mathcal{L}_o = \left\| \Downarrow^3(I^{SR}) - I^{LR} \right\|_1, \quad (15)$$

where \Downarrow^3 is the bicubic downsampling operator.

- GAN Loss [16]:

The discriminator loss is:

$$\mathcal{L}_D = -\log(D(I^{SR})), \quad (16)$$

where D represents the discriminator network. The generator loss is:

$$\mathcal{L}_{GAN} = -\log(D(I^{HR})) - \log(1 - D(I^{SR})). \quad (17)$$

- SSIM [55] Loss:

$$\mathcal{L}_{SSIM} = 1 - \frac{(2\mu_{I^{SR}}\mu_{I^{HR}} + C_1)(2\sigma_{I^{SR}I^{HR}} + C_2)}{(\mu_{I^{SR}}^2 + \mu_{I^{HR}}^2 + C_1)(\sigma_{I^{SR}} + \sigma_{I^{HR}} + C_2)}, \quad (18)$$

where $\mu_{I^{SR}}$ and $\mu_{I^{HR}}$ are the mean values of I^{SR} and I^{HR} , $\sigma_{I^{SR}}$ and $\sigma_{I^{HR}}$ are the standard deviations of I^{SR} and I^{HR} , $\sigma_{I^{SR}I^{HR}}$ is the covariance between I^{SR} and I^{HR} , C_1 and C_2 are small constants to stabilize the division.

- LPIPS [58] Loss:

$$\mathcal{L}_{LPIPS} = \sum_{l \in F} w_l \left\| \phi_l(I^{SR}) - \phi_l(I^{HR}) \right\|_2^2, \quad (19)$$

where F represents the set of intermediate layers in the chosen neural network, ϕ_l is the normalized outputs of layer l for images, w_l are the official weights determined by Zhang et al. [58].

Datasets. The DIV2K [1] training set (800 images) was employed for training. For testing, we utilize a collection of datasets including Set5 [3], Set14 [56], DIV2K [1] validation set, BSD100 [32], Urban100



Figure 4: Visual comparison of three sampled points on the Pareto frontier obtained through our method (as defined in Figure 1), alongside other artworks, on the Urban100 [17] dataset. More visual results are presented in the supplementary material.

[17], General100 [12], and Manga109 [33]. We followed the previous work [26, 31, 36, 53] to focus only on $\times 4$ super-resolution to train and evaluate the effectiveness of our SR model. Specifically, we obtain the LR images by downsampling the HR counterparts by a factor of 4 using bicubic interpolation.

Training Details. We randomly sample 16 patches from each image as a batch, the patch size of LR is 32×32 . To ensure stability in the SR model training progress and MOBO optimization process, we initially pre-train for 250 epochs using manually set loss weights from ESRGAN [53], defined as:

$$\mathcal{L} = \omega_1 \mathcal{L}_1 + \omega_{\phi_5} \mathcal{L}_{\phi_5} + \omega_{GAN} \mathcal{L}_{GAN}, \quad (20)$$

where $[\omega_1, \omega_{\phi_5}, \omega_{GAN}] = [1e-2, 1, 5e-3]$. Subsequently, we commence loss weight optimization using our MOBO method. The learning rate during pre-training is fixed at $1e-4$, and for optimization with MOBO, the initial learning rate is set at $5e-5$ and is halved every 250 epochs. The optimizer employed is Adam [21]. Our SR model is implemented by PyTorch [39] on NVIDIA RTX 3090 GPUs, and MOBO is realized through the Ax platform [2].

4.2 Quantitative Results

Methods utilize RRDB [53] as the backbone, and aim to address the balance between perceptual quality and distortion are selected for fair comparisons. To this end, to the best of our knowledge, all five publicly available artworks are used for comparison: ESRGAN [53], SPSR [31], RRDB+LDL [26], CAL-GAN [36] and SROOE [37].

All of which utilize RRDB [53] as their backbones. It is noteworthy that SROOE [37] is trained on the larger DF2K dataset (3450 images), which consists of the DIV2K [1] training set (800 images) and Flickr2K [45] (2650 images). ESRGAN [53], on the other hand, is trained on the even larger DF2K-OST dataset (13774 images), which includes DF2K (3450 images) and OST [51] (10,324 images). Additionally, the SPSR [31] network incorporates an extra gradient branch, and SROOE [37] introduces an auxiliary network to predict a discrete set of predefined loss weight combinations. These two methods introduce additional computational load during inference.

We incorporated all the loss functions introduced in Section 4.1 and optimized their weights using the MOBO strategy. Our optimization objectives were PSNR and LPIPS [58]. The loss function is formulated as:

$$\begin{aligned} \mathcal{L} = & \omega_1 \mathcal{L}_1 + \omega_2 \mathcal{L}_2 + \omega_{FFT} \mathcal{L}_{FFT} + \omega_{\nabla} \mathcal{L}_{\nabla} + \\ & \omega_{\phi_2} \mathcal{L}_{\phi_2} + \omega_{\phi_3} \mathcal{L}_{\phi_3} + \omega_{\phi_4} \mathcal{L}_{\phi_4} + \omega_{\phi_5} \mathcal{L}_{\phi_5} + \\ & \omega_{\circ} \mathcal{L}_{\circ} + \omega_{GAN} \mathcal{L}_{GAN} + \omega_{SSIM} \mathcal{L}_{SSIM} + \\ & \omega_{LPIPS} \mathcal{L}_{LPIPS}. \end{aligned} \quad (21)$$

And the optimization formula is:

$$[PSNR, LPIPS] = f([\omega_1, \omega_2, \omega_{FFT}, \omega_{\nabla}, \omega_{\phi_2}, \omega_{\phi_3}, \omega_{\phi_4}, \omega_{\phi_5}, \omega_{\circ}, \omega_{GAN}, \omega_{SSIM}, \omega_{LPIPS}]). \quad (22)$$

As demonstrated in Table 1, except for SROOE [37], our approach not only demonstrates superior performance in the full-reference perceptual metric (LPIPS [58]) but also significantly surpasses other

Table 2: Ablation study on 7 datasets compares MOBO-optimized loss weights to ESRGAN [53] manually-set loss weights. Both models use the official ESRGAN [53] train code and are trained on the DIV2K [1] training set with the same settings, except that the loss weights for MOBOSR are optimized by MOBO. The best results are highlighted in bold. MOBOSR consistently outperforms ESRGAN [53] by a large margin in the same setting. This comparison intuitively demonstrates the effectiveness of the core idea of our work: automatic loss weight optimization.

Metrics	Methods	Set5	Set14	DIV2K	BSD100	Urban100	General100	Manga109
PSNR↑	ESRGAN [53]	29.8023	25.5164	27.6994	25.2100	23.7431	28.8618	27.3669
	MOBOSR (Ours)	30.6926	26.8148	28.5089	26.0402	24.4895	29.6640	28.2091
SSIM↑	ESRGAN [53]	0.8456	0.6855	0.7610	0.6463	0.7116	0.7979	0.8436
	MOBOSR (Ours)	0.8607	0.7234	0.7834	0.6781	0.7357	0.8209	0.8621
LR-PSNR↑	ESRGAN [53]	42.5573	38.2986	41.2244	40.3034	37.6727	41.6356	40.0483
	MOBOSR (Ours)	44.6401	43.0412	44.6847	43.5394	41.8108	44.6812	43.1860
LPIPS↓	ESRGAN [53]	0.0742	0.1689	0.1193	0.1751	0.1379	0.0943	0.0748
	MOBOSR (Ours)	0.0745	0.1359	0.1145	0.1719	0.1324	0.0894	0.0675

methods in distortion metrics (PSNR and SSIM [55]) and consistency metric (LR-PSNR). Compared to SROOE [37], we achieve superior performance on all distortion metrics with similar LPIPS [58], even though we only train on the smaller DIV2K [1] training set. This indicates that our approach not only achieves excellent perceptual metrics but also mitigates the artifacts and false textures introduced by perceptual loss [19] and GAN [16], thereby ensuring consistency with the LR source and the pixel accuracy with the HR image. In summary, our method consistently outperforms others in both distortion and perceptual quality, demonstrating that the integration of MOBO facilitates the attainment of the Pareto frontier (optimal balance boundary) for perception quality and distortion.

Furthermore, prior to our work, manually setting such a multitude of loss weights is impractical, which consequently limits the incorporation of additional loss functions into the SISR model. While our method can efficiently and autonomously determine the optimal weights for loss functions, without introducing any additional computations during the inference and significantly extending the training duration (time consuming about SR model and MOBO during training are detailed in the supplementary material).

4.3 Qualitative Results

Visual comparisons of Ours-[a,b,c] (as defined in Figure 1), as depicted in Figure 4, clearly reveal the inherent contradiction between perception quality and distortion. This is evidenced by the gradual deterioration in PSNR and the corresponding improvement in LPIPS [58] on the Pareto frontier. A higher PSNR typically results in a more blurred image, albeit with reduced noise and artifacts. Conversely, a better LPIPS [58] score indicates a sharper image, which, however, tends to introduce noise and artifacts. Compared to other methods, our approach generates fewer noise and artifacts without excessively blurring the image. Additionally, it exhibits more accurate reconstruction in certain areas, better preserving the original structure of the objects in image.

4.4 Ablation Study

To demonstrate the effectiveness of using MOBO to optimize loss weights compared to manually set loss weights, we conduct a comparative experiment. Our setup is identical to that of ESRGAN [53],

with the exception that the loss weights are optimized by MOBO. Our optimization formula is expressed as:

$$[PSNR, LPIPS] = f([\omega_1, \omega_{\phi_s}, \omega_{GAN}]). \quad (23)$$

The loss weights for ESRGAN [53] are adopted from the weights utilized by the authors in the original publication: $[\omega_1, \omega_{\phi_s}, \omega_{GAN}] = [1e - 2, 1, 5e - 3]$. As demonstrated in Table 2, our approach significantly surpasses ESRGAN [53] across all metrics, which is retrained on the DIV2K [1] training set using the official released codes. This experiment clearly demonstrates the substantial advantages of integrating MOBO for automatically optimizing loss weights in the SR model over the manual tuning of loss weights.

From the comparison between ‘MOBOSR (Ours)’ in Table 2 and ‘Ours-c’ in Table 1, it is evident that incorporating a greater variety of loss functions significantly benefits the SISR model, provided that the weights for these losses are optimally set.

5 Conclusion

In this research, we propose the Multi-Objective Bayesian Optimization Super-Resolution (MOBOSR). To effectively address the balance between perceptual quality and distortion, we introduce multi-objective Bayesian optimization into the single-image super-resolution model, dynamically adjusting the weights of various loss functions during training. Our method is rigorously validated through comprehensive experiments, demonstrating its effectiveness and versatility in both distortion and perceptual quality. Given its potential to be applied to nearly all domains of image restoration and enhancement, we believe our method can offer valuable insights and contributions to the community.

Acknowledgments

This work was supported in part by the Key Laboratory of Smart Earth under Grant KF2023YB01-13, and in part by the National Natural Science Foundation of China (NSFC) under Grant 62176100. The computation is completed in the HPC Platform of Huazhong University of Science and Technology.

References

- [1] Eirikur Agustsson and Radu Timofte. 2017. NTIRE 2017 Challenge on Single Image Super-Resolution: Dataset and Study. In *Proceedings of the IEEE/CVF Conference on Computer Vision and Pattern Recognition Workshops (CVPRW)*. 1122–1131.
- [2] Eytan Bakshy, Lili Dworkin, Brian Karrer, Konstantin Kashin, Ben Letham, Ashwin Murthy, and Shaun Singh. 2018. AE: A domain-agnostic platform for adaptive experimentation. In *Proceedings of the Advances in Neural Information Processing Systems Workshops (NeurIPS)*.
- [3] Marco Bevilacqua, Aline Roumy, Christine M. Guillemot, and Marie-Line Alberi-Morel. 2012. Low-Complexity Single-Image Super-Resolution based on Nonnegative Neighbor Embedding. In *Proceedings of the British Machine Vision Conference (BMVC)*.
- [4] Yochai Blau, Roey Mechrez, Radu Timofte, Tomer Michaeli, and Lihl Zelnik-Manor. 2019. The 2018 PIRM Challenge on Perceptual Image Super-Resolution. In *Proceedings of the European Conference on Computer Vision Workshops (ECCVW)*. 334–355.
- [5] Yochai Blau and Tomer Michaeli. 2018. The Perception-Distortion Tradeoff. In *Proceedings of the IEEE/CVF Conference on Computer Vision and Pattern Recognition (CVPR)*. 6228–6237.
- [6] Manri Cheon, Jun-Hyuk Kim, Jun-Ho Choi, and Jong-Seok Lee. 2019. Generative Adversarial Network-Based Image Super-Resolution Using Perceptual Content Losses. In *Proceedings of the European Conference on Computer Vision Workshops (ECCVW)*. 51–62.
- [7] Samuel Daulton, Maximilian Balandat, and Eytan Bakshy. 2020. Differentiable Expected Hypervolume Improvement for Parallel Multi-Objective Bayesian Optimization. In *Proceedings of the Advances in Neural Information Processing Systems (NeurIPS)*, Vol. 33. 9851–9864.
- [8] Samuel Daulton, Maximilian Balandat, and Eytan Bakshy. 2021. Parallel Bayesian Optimization of Multiple Noisy Objectives with Expected Hypervolume Improvement. In *Proceedings of the Advances in Neural Information Processing Systems (NeurIPS)*, Vol. 34. 2187–2200.
- [9] Kalyanmoy Deb, Amrit Pratap, Sameer Agarwal, and T. Meyarivan. 2002. A Fast and Elitist Multiobjective Genetic Algorithm: NSGA-II. *IEEE Transactions on Evolutionary Computation* 6, 2 (2002), 182–197.
- [10] Xin Deng, Ren Yang, Mai Xu, and Pier Luigi Dragotti. 2019. Wavelet Domain Style Transfer for an Effective Perception-Distortion Tradeoff in Single Image Super-Resolution. In *Proceedings of the IEEE/CVF International Conference on Computer Vision (ICCV)*. 3076–3085.
- [11] Chao Dong, Chen Change Loy, Kaiming He, and Xiaoou Tang. 2014. Learning a Deep Convolutional Network for Image Super-Resolution. In *Proceedings of the European Conference on Computer Vision (ECCV)*. 184–199.
- [12] Chao Dong, Chen Change Loy, and Xiaoou Tang. 2016. Accelerating the Super-Resolution Convolutional Neural Network. In *Proceedings of the European Conference on Computer Vision (ECCV)*. 391–407.
- [13] Michael T. M. Emmerich, Kyriakos C. Giannakoglou, and Boris Naujoks. 2006. Single- and Multiobjective Evolutionary Optimization Assisted by Gaussian Random Field Metamodels. *IEEE Transactions on Evolutionary Computation* 10, 4 (2006), 421–439.
- [14] Manuel Fritsche, Shuhang Gu, and Radu Timofte. 2019. Frequency Separation for Real-World Super-Resolution. In *Proceedings of the IEEE/CVF International Conference on Computer Vision Workshops (ICCVW)*. 3599–3608.
- [15] Dario Fuoli, Luc Van Gool, and Radu Timofte. 2021. Fourier Space Losses for Efficient Perceptual Image Super-Resolution. In *Proceedings of the IEEE/CVF International Conference on Computer Vision (ICCV)*. 2340–2349.
- [16] Ian Goodfellow, Jean Pouget-Abadie, Mehdi Mirza, Bing Xu, David Warde-Farley, Sherjil Ozair, Aaron Courville, and Yoshua Bengio. 2020. Generative adversarial networks. *Commun. ACM* 63, 11 (oct 2020), 139–144.
- [17] Jia-Bin Huang, Abhishek Singh, and Narendra Ahuja. 2015. Single Image Super-Resolution From Transformed Self-Exemplars. In *Proceedings of the IEEE/CVF Conference on Computer Vision and Pattern Recognition (CVPR)*. 5197–5206.
- [18] Sergey Ioffe and Christian Szegedy. 2015. Batch Normalization: Accelerating Deep Network Training by Reducing Internal Covariate Shift. In *Proceedings of the International Conference on Machine Learning (ICML)*, Vol. 37. 448–456.
- [19] Justin Johnson, Alexandre Alahi, and Li Fei-Fei. 2016. Perceptual Losses for Real-Time Style Transfer and Super-Resolution. In *Proceedings of the European Conference on Computer Vision (ECCV)*. 694–711.
- [20] Donald R. Jones, Matthias Schonlau, and William J. Welch. 1998. Efficient Global Optimization of Expensive Black-Box Functions. *Journal of Global Optimization* 13, 4 (01 Dec 1998), 455–492.
- [21] Diederik P. Kingma and Jimmy Ba. 2017. Adam: A Method for Stochastic Optimization. In *Proceedings of the International Conference on Learning Representations (ICLR)*.
- [22] Wei-Sheng Lai, Jia-Bin Huang, Narendra Ahuja, and Ming-Hsuan Yang. 2017. Deep Laplacian Pyramid Networks for Fast and Accurate Super-Resolution. In *Proceedings of the IEEE/CVF Conference on Computer Vision and Pattern Recognition (CVPR)*. 5835–5843.
- [23] Iro Laina, Christian Rupprecht, Vasileios Belagiannis, Federico Tombari, and Nassir Navab. 2016. Deeper Depth Prediction with Fully Convolutional Residual Networks. In *Proceedings of the International Conference on 3D Vision (3DV)*. 239–248.
- [24] Christian Ledig, Lucas Theis, Ferenc Huszar, Jose Caballero, Andrew Cunningham, Alejandro Acosta, Andrew Aitken, Alykhan Tejani, et al. 2017. Photo-Realistic Single Image Super-Resolution Using a Generative Adversarial Network. In *Proceedings of the IEEE/CVF Conference on Computer Vision and Pattern Recognition (CVPR)*. 105–114.
- [25] Jingyun Liang, Jie Zhang, Guolei Sun, Kai Zhang, Luc Van Gool, and Radu Timofte. 2021. SwinIR: Image Restoration Using Swin Transformer. In *Proceedings of the IEEE/CVF International Conference on Computer Vision Workshops (ICCVW)*. 1833–1844.
- [26] Jie Liang, Hui Zeng, and Lei Zhang. 2022. Details or Artifacts: A Locally Discriminative Learning Approach to Realistic Image Super-Resolution. In *Proceedings of the IEEE/CVF Conference on Computer Vision and Pattern Recognition (CVPR)*. 5657–5666.
- [27] Bee Lim, Sanghyun Son, Heewon Kim, Seungjun Nah, and Kyoung Mu Lee. 2017. Enhanced Deep Residual Networks for Single Image Super-Resolution. In *Proceedings of the IEEE/CVF Conference on Computer Vision and Pattern Recognition Workshops (CVPRW)*. 1132–1140.
- [28] Tao Liu, Jun Cheng, and Shan Tan. 2023. Spectral Bayesian Uncertainty for Image Super-Resolution. In *Proceedings of the IEEE/CVF Conference on Computer Vision and Pattern Recognition (CVPR)*. 18166–18175.
- [29] Ze Liu, Yutong Lin, Yue Cao, Han Hu, Yixuan Wei, Zheng Zhang, Stephen Lin, and Baining Guo. 2021. Swin Transformer: Hierarchical Vision Transformer using Shifted Windows. In *Proceedings of the IEEE/CVF International Conference on Computer Vision (ICCV)*. 9992–10002.
- [30] Abrahamyan Lusine, Truong Anh Minh, Philips Wilfried, and Deligiannis Nikos. 2022. Gradient Variance Loss for Structure-Enhanced Image Super-Resolution. *Proceedings of the International Conference on Acoustics, Speech, and Signal Processing (ICASSP)* (2022).
- [31] Cheng Ma, Yongming Rao, Yean Cheng, Ce Chen, Jiwen Lu, and Jie Zhou. 2020. Structure-Preserving Super Resolution With Gradient Guidance. In *Proceedings of the IEEE/CVF Conference on Computer Vision and Pattern Recognition (CVPR)*. 7766–7775.
- [32] David Martin, Charless Fowlkes, Doron Tal, and Jitendra Malik. 2001. A Database of Human Segmented Natural Images and Its Application to Evaluating Segmentation Algorithms and Measuring Ecological Statistics. In *Proceedings of the IEEE/CVF International Conference on Computer Vision (ICCV)*, Vol. 2. 416–423.
- [33] Yusuke Matsui, Kota Ito, Yuji Aramaki, Azuma Fujimoto, Toru Ogawa, Toshihiko Yamasaki, and Kiyoharu Aizawa. 2017. Sketch-Based Manga Retrieval Using Manga109 Dataset. *Multimedia Tools and Applications* 76, 20 (01 Oct 2017), 21811–21838.
- [34] Pablo Navarrete Michelini, Dan Zhu, and Hanwen Liu. 2019. Multi-scale Recursive and Perception-Distortion Controllable Image Super-Resolution. In *Proceedings of the European Conference on Computer Vision Workshops (ECCVW)*. 3–19.
- [35] A.J. Nebro, J.J. Durillo, J. Garcia-Nieto, C.A. Coello Coello, F. Luna, and E. Alba. 2009. SMPSO: A New PSO-Based Metaheuristic for Multi-Objective Optimization. In *Proceedings of the IEEE Symposium on Computational Intelligence in Multi-Criteria Decision-Making (MCDM)*. 66–73.
- [36] Joonkyu Park, Sanghyun Son, and Kyoung Mu Lee. 2023. Content-Aware Local GAN for Photo-Realistic Super-Resolution. In *Proceedings of the IEEE/CVF International Conference on Computer Vision (ICCV)*. 10585–10594.
- [37] Seung Ho Park, Young Su Moon, and Nam Ik Cho. 2023. Perception-Oriented Single Image Super-Resolution using Optimal Objective Estimation. In *Proceedings of the IEEE/CVF Conference on Computer Vision and Pattern Recognition (CVPR)*. 1725–1735.
- [38] Seong-Jin Park, Hyeonseok Son, Sunghyun Cho, Ki-Sang Hong, and Seungyong Lee. 2018. SRFeat: Single Image Super-Resolution with Feature Discrimination. In *Proceedings of the European Conference on Computer Vision (ECCV)*. 455–471.
- [39] Adam Paszke, Sam Gross, Francisco Massa, Adam Lerer, James Bradbury, Gregory Chanan, Trevor Killeen, Zeming Lin, et al. 2019. PyTorch: An Imperative Style, High-Performance Deep Learning Library. In *Proceedings of the Advances in Neural Information Processing Systems (NeurIPS)*. 8024–8035.
- [40] Mohammad Saeed Rad, Behzad Bozorgtabar, Urs-Viktor Marti, Max Basler, Hazim Kemal Ekenel, and Jean-Philippe Thiran. 2019. SROBB: Targeted Perceptual Loss for Single Image Super-Resolution. In *Proceedings of the IEEE/CVF International Conference on Computer Vision (ICCV)*. 2710–2719.
- [41] Mehdi S. M. Sajjadi, Bernhard Schölkopf, and Michael Hirsch. 2017. EnhanceNet: Single Image Super-Resolution Through Automated Texture Synthesis. In *Proceedings of the IEEE/CVF International Conference on Computer Vision (ICCV)*. 4501–4510.
- [42] Wenzhe Shi, Jose Caballero, Ferenc Huszar, Johannes Totz, Andrew P. Aitken, Rob Bishop, Daniel Rueckert, and Zehan Wang. 2016. Real-Time Single Image and Video Super-Resolution Using an Efficient Sub-Pixel Convolutional Neural Network. In *Proceedings of the IEEE/CVF Conference on Computer Vision and*

- Pattern Recognition (CVPR)*. 1874–1883.
- [43] Karen Simonyan and Andrew Zisserman. 2015. Very Deep Convolutional Networks for Large-Scale Image Recognition. In *Proceedings of the International Conference on Learning Representations (ICLR)*.
- [44] Long Sun, Jinshan Pan, and Jinhui Tang. 2022. ShuffleMixer: An Efficient ConvNet for Image Super-Resolution. In *Proceedings of the Advances in Neural Information Processing Systems (NeurIPS)*, Vol. 35. 17314–17326.
- [45] Radu Timofte, Eirikur Agustsson, Luc Van Gool, Ming-Hsuan Yang, Lei Zhang, Bee Lim, Sanghyun Son, Heewon Kim, Seungjun Nah, et al. 2017. NTIRE 2017 Challenge on Single Image Super-Resolution: Methods and Results. In *Proceedings of the IEEE/CVF Conference on Computer Vision and Pattern Recognition Workshops (CVPRW)*. 1110–1121.
- [46] Rao Muhammad Umer and Christian Micheloni. 2020. Deep Cyclic Generative Adversarial Residual Convolutional Networks for Real Image Super-Resolution. In *Proceedings of the European Conference on Computer Vision (ECCV)*. 484–498.
- [47] Thang Vu, Tung M. Luu, and Chang D. Yoo. 2019. Perception-Enhanced Image Super-Resolution via Relativistic Generative Adversarial Networks. In *Proceedings of the European Conference on Computer Vision Workshops (ECCVW)*. 98–113.
- [48] Tobias Wagner, Michael Emmerich, André Deutz, and Wolfgang Ponweiser. 2010. On Expected-Improvement Criteria for Model-based Multi-objective Optimization. In *Proceedings of the Parallel Problem Solving from Nature (PPSN)*. 718–727.
- [49] Chenyang Wang, Junjun Jiang, Zhiwei Zhong, and Xianming Liu. 2023. Spatial-Frequency Mutual Learning for Face Super-Resolution. In *Proceedings of the IEEE/CVF Conference on Computer Vision and Pattern Recognition (CVPR)*. 22356–22366.
- [50] Wei Wang, Ruiming Guo, Yapeng Tian, and Wenming Yang. 2019. CFSNet: Toward a Controllable Feature Space for Image Restoration. In *Proceedings of the IEEE/CVF International Conference on Computer Vision (ICCV)*. 4139–4148.
- [51] Xintao Wang, Ke Yu, Chao Dong, and Chen Change Loy. 2018. Recovering Realistic Texture in Image Super-Resolution by Deep Spatial Feature Transform. In *Proceedings of the IEEE/CVF Conference on Computer Vision and Pattern Recognition (CVPR)*. 606–615.
- [52] Xintao Wang, Ke Yu, Chao Dong, Xiaoou Tang, and Chen Change Loy. 2019. Deep Network Interpolation for Continuous Imagery Effect Transition. In *Proceedings of the IEEE/CVF Conference on Computer Vision and Pattern Recognition (CVPR)*. 1692–1701.
- [53] Xintao Wang, Ke Yu, Shixiang Wu, Jinjin Gu, Yihao Liu, Chao Dong, Yu Qiao, and Chen Change Loy. 2019. ESRGAN: Enhanced Super-Resolution Generative Adversarial Networks. In *Proceedings of the European Conference on Computer Vision (ECCV)*. 63–79.
- [54] Yan Wang. 2022. Edge-enhanced Feature Distillation Network for Efficient Super-Resolution. In *Proceedings of the IEEE/CVF Conference on Computer Vision and Pattern Recognition Workshops (CVPRW)*. 776–784.
- [55] Zhou Wang, A.C. Bovik, H.R. Sheikh, and E.P. Simoncelli. 2004. Image Quality Assessment: from Error Visibility to Structural Similarity. *IEEE Transactions on Image Processing* 13, 4 (2004), 600–612.
- [56] Roman Zeyde, Michael Elad, and Matan Protter. 2012. On Single Image Scale-Up Using Sparse-Representations. In *Proceedings of the International Conference on Curves and Surfaces*. 711–730.
- [57] Qingfu Zhang and Hui Li. 2007. MOEA/D: A Multiobjective Evolutionary Algorithm Based on Decomposition. *IEEE Transactions on Evolutionary Computation* 11, 6 (2007), 712–731.
- [58] Richard Zhang, Phillip Isola, Alexei A. Efros, Eli Shechtman, and Oliver Wang. 2018. The Unreasonable Effectiveness of Deep Features as a Perceptual Metric. In *Proceedings of the IEEE/CVF Conference on Computer Vision and Pattern Recognition (CVPR)*. 586–595.
- [59] Eckart Zitzler, Marco Laumanns, and Lothar Thiele. 2001. SPEA2: Improving the strength pareto evolutionary algorithm. *Technical Report Gloriatrasse* (2001).

Supplementary Materials: Perceptual Oriented Image Restoration is a Multi-Objective Optimization Problem

Qiwen Zhu

State Key Lab of MIIPT, Huazhong
University of Science and Technology
Wuhan, China
zhuqiwen@hust.edu.cn

Yanjie Wang

School of AIA, Huazhong University
of Science and Technology
Wuhan, China
aiawyj@hust.edu.cn

Shilv Cai

School of AIA, Huazhong University
of Science and Technology
Wuhan, China
caishilv@hust.edu.cn

Liqun Chen

School of AIA, Huazhong University
of Science and Technology
Wuhan, China
chenliqun@hust.edu.cn

Jiahuan Zhou

Wangxuan Institute of Computer
Technology, Peking University
Beijing, China
jiahuanzhou@pku.edu.cn

Luxin Yan

State Key Lab of MIIPT, Huazhong
University of Science and Technology
Wuhan, China
yanluxin@hust.edu.cn

Sheng Zhong

State Key Lab of MIIPT, Huazhong
University of Science and Technology
Wuhan, China
zhongsheng@hust.edu.cn

Xu Zou*

State Key Lab of MIIPT, Huazhong
University of Science and Technology
Wuhan, China
zoux@hust.edu.cn

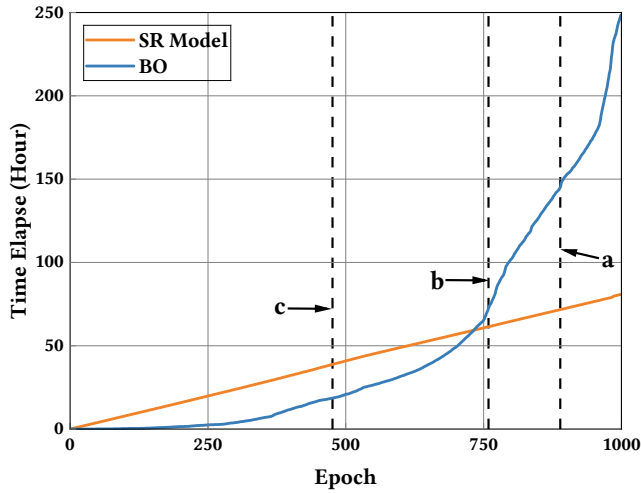


Figure 1: Comparative of the time consumed for training the SR model against the time required for BO during the training process of our MOBOSR. The temporal measurements were conducted on an server with NVIDIA RTX 3090 GPU and two Intel Xeon Gold 6226R CPUs. Epochs for Ours-[a,b,c] are labeled for clarity.

1 Time Analysis

Bayesian Optimization (BO) minimizes the number of evaluations by substituting the actual objective function with a surrogate function and heuristically determining the most promising points for improvement through an acquisition function for subsequent evaluation rounds. Consequently, this approach significantly conserves

*Corresponding author.

Table 1: Detailed comparison of time expended for sampling points Ours-[a,b,c] and at the optimization cessation.

Point	Epoch	SR Time Elapse	MOBO Time Elapse
Ours-c	476	38.8h	18.6h
Ours-b	759	61.4h	72.6h
Ours-a	889	71.7h	145.2h
End	1000	80.8h	248.4h

optimization iteration compared to evolutionary algorithms. However, the BO process necessitates the computation of the covariance matrix, resulting in a time complexity of $O(n^3)$. If the objective function be overly intricate or the problem dimensions too high, necessitating numerous optimization rounds, this would substantially increase the optimization time.

In the main text, the three sampling points selected from the perceptual-distortion Pareto front, labeled as Ours-[a,b,c], were obtained at epochs 476, 759 and 889, respectively. As shown in Table 1 and Figure 1, the time consumed to train the Super-Resolution (SR) model with Ours-c, obtained at epoch 476, was approximately half of that required for BO. At epoch 759, the training time for the SR model with Ours-b was nearly identical to that for BO. However, by epoch 889, the time expended on BO for Ours-a was roughly half of that for training the SR model. By the designated optimization halt at epoch 1000, the time consumption for BO had become threefold that of the SR model.

But, after optimization up to epoch 759 (Ours-c), there were no significant changes in the Pareto front (as shown in Figure 2). We believe that the substantial advantages brought by our Multi-Objective Bayesian Optimization Super-Resolution (MOBOSR), and without introducing any additional computational load during inference, justify the mere doubling of training duration.

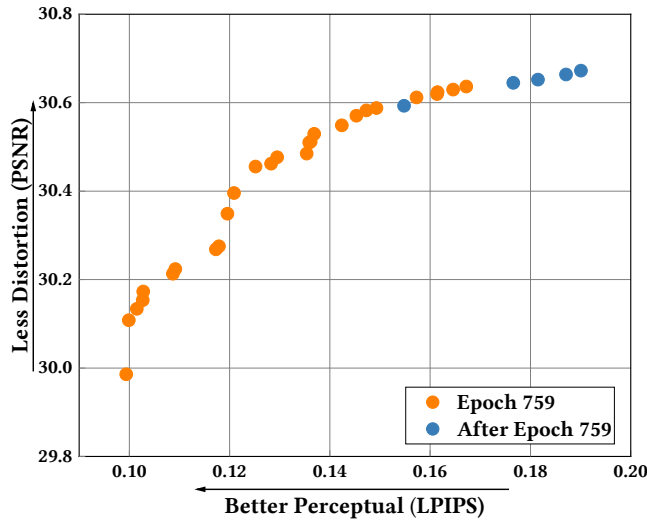


Figure 2: Changes in the perception-distortion Pareto frontier obtained by our MOBOSR after epoch 759.

Table 2: Analyses of multi-task learning on the DIV2K [1] validation set. The best and second-best results are highlighted in bold and underline, respectively. MTL methods show significant improvements over the manually weighted ESRGAN [12] but are not as effective as our MOBOSR.

Methods	PSNR \uparrow	SSIM \uparrow	LR-PSNR \uparrow	LPIPS \downarrow
ESRGAN [12]	27.6994	0.7610	41.2244	0.1193
CAGrad [5]	<u>28.4434</u>	<u>0.7803</u>	47.5291	<u>0.1161</u>
NashMTL [7]	28.1606	0.7717	43.7037	0.1168
MOBOSR (Ours)	28.5089	0.7834	<u>44.6847</u>	0.1145

2 Discussion on Multi-Task Learning

Focusing on a single task may overlook the information from related tasks that could improve the target task. By sharing parameters between different tasks (with different loss functions) to a certain extent may achieve better generalization for the original task. Hence, we discuss the impact of Multi-Task Learning (MTL) in balancing the distortion and perceptual quality for SISR models. We initially consider using MTL to optimize multiple loss functions to address the balance issue. We compare the results of our MOBOSR with 2 MTL methods (CAGrad [5] and NashMTL [7]), as well as with ESRGAN [12]. As shown in Table 2, MTL methods show significant improvements over the manually weighted ESRGAN [12] but are not as effective as our MOBOSR. We believe this is because MTL approaches just seek a single compromise between multi-task/multi-loss rather than searching for the entire Pareto frontier as MOBO does. But, the ability to achieve these outcomes indicates that MTL merits further investigation.

3 Metrics Recalculation Details

Due to the variations in datasets and metrics reported by the methods under comparison, as well as the differences in implementation

details during metric computation, we have adopted a uniform metric calculation method to re-evaluate the metrics of other methods. This ensures a fairer comparison. We generated SR results for all test sets using the model weights and inference code released by the authors, followed by calculations using our standardized metric computation program. Our codes for metric calculation are detailed in the GitHub repository: <https://github.com/ZhuKeven/MOBOSR>. Table 3 presents the metrics we recomputed alongside those reported by the authors, with most showing no significant differences and some even surpassing the reported results. Wang et al. only reported metrics for the RRDB-PSNR [12] model trained with L1 loss, without providing the metrics for the ESRGAN [12] model trained using GAN [2]. Consequently, we are unable to present the ESRGAN [12] metrics comparison in Table 3 in the same manner as for other methods.

4 More Quantitative Results

Due to the length constraints of the main text, we have included the complete results for Ours-[a,b,c] here, as well as the metrics for the RRDB-PSNR [12] model trained using L1 loss. Although RRDB-PSNR [12] exhibits superior performance in terms of PSNR and SSIM [13] metrics, the margin by which it surpasses Ours-a is considerably less than the extent to which Ours-a exceeds RRDB-PSNR [12] in perceptual (LPIPS) and consistency (LR-PSNR) metrics. Not to mention that the RRDB-PSNR [12] was trained on a significantly larger dataset, the DF2K-OST (13774 images), which comprises the DIV2K [1] training set (800 images), Flickr2K [10] (2650 images), and OST [11] (10,324 images), whereas our MOBOSR was trained solely on the DIV2K [1] training set (800 images).

5 More Visual Results

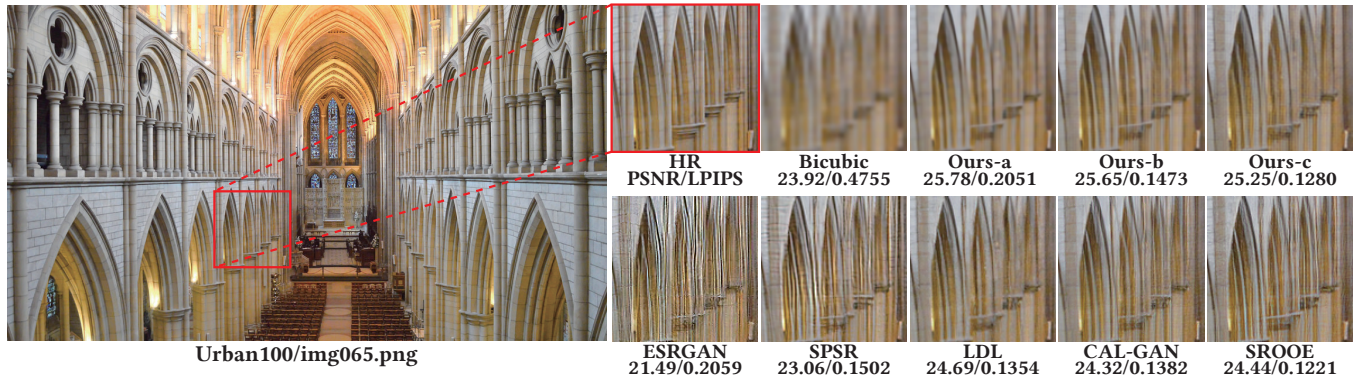
We have included more visual comparison results here, including the visualizations on the Urban100 [3] dataset as shown in Figure 3 and Figure 4, and the visualizations on the DIV2K [1] validation set as shown in Figure 5.

References

- [1] Eirikur Agustsson and Radu Timofte. 2017. NTIRE 2017 Challenge on Single Image Super-Resolution: Dataset and Study. In *Proceedings of the IEEE/CVF Conference on Computer Vision and Pattern Recognition Workshops (CVPRW)*, 1122–1131.
- [2] Ian Goodfellow, Jean Pouget-Abadie, Mehdi Mirza, Bing Xu, David Warde-Farley, Sherjil Ozair, Aaron Courville, and Yoshua Bengio. 2020. Generative adversarial networks. *Commun. ACM* 63, 11 (oct 2020), 139–144.
- [3] Jia-Bin Huang, Abhishek Singh, and Narendra Ahuja. 2015. Single Image Super-Resolution From Transformed Self-Exemplars. In *Proceedings of the IEEE/CVF Conference on Computer Vision and Pattern Recognition (CVPR)*, 5197–5206.
- [4] Jie Liang, Hui Zeng, and Lei Zhang. 2022. Details or Artifacts: A Locally Discriminative Learning Approach to Realistic Image Super-Resolution. In *Proceedings of the IEEE/CVF Conference on Computer Vision and Pattern Recognition (CVPR)*, 5657–5666.
- [5] Bo Liu, Xingchao Liu, Xiaojie Jin, Peter Stone, and Qiang Liu. 2021. Conflict-Averse Gradient Descent for Multi-task Learning. In *Proceedings of the Advances in Neural Information Processing Systems (NeurIPS)*, Vol. 34, 18878–18890.
- [6] Cheng Ma, Yongming Rao, Yean Cheng, Ce Chen, Jiwen Lu, and Jie Zhou. 2020. Structure-Preserving Super Resolution With Gradient Guidance. In *Proceedings of the IEEE/CVF Conference on Computer Vision and Pattern Recognition (CVPR)*, 7766–7775.
- [7] Aviv Navon, Aviv Shamsian, Idan Achituve, Haggai Maron, Kenji Kawaguchi, Gal Chechik, and Ethan Fetaya. 2022. Multi-Task Learning as a Bargaining Game. In *Proceedings of the International Conference on Machine Learning (ICML)*, Vol. 162, 16428–16446.
- [8] Joonkyu Park, Sanghyun Son, and Kyoung Mu Lee. 2023. Content-Aware Local GAN for Photo-Realistic Super-Resolution. In *Proceedings of the IEEE/CVF*

Table 3: Comparison of metrics calculated using our uniform method versus those reported by the authors, showing minimal difference, with some even surpassing the reported results. The higher results are highlighted in bold. The symbols \uparrow and \downarrow indicate that higher or lower values of the metric are preferable.

Metric	Dataset	RRDB-PSNR [12]		SPSR [6]		RRDB+LDL [4]		CAL-GAN [8]		SROOE [9]	
		Author	Recalculated	Author	Recalculated	Author	Recalculated	Author	Recalculated	Author	Recalculated
PSNR \uparrow	Set5	32.73	32.7010	30.400	30.3871	30.985	31.0007	31.177	31.0475	-	31.2455
	Set14	28.99	28.9831	26.640	26.6501	27.491	27.2064	-	27.3272	-	27.2561
	DIV2K	-	30.8888	-	28.1824	28.951	28.9510	28.863	28.9549	27.69	29.0990
	BSD100	27.85	27.8235	25.505	25.4949	-	26.0988	25.925	26.2581	24.87	26.1715
	Urban100	27.03	26.9859	24.799	24.8063	25.498	25.4781	25.290	25.2908	24.33	25.8452
	General100	-	31.9145	29.414	29.4794	30.232	30.1974	30.182	30.0742	28.74	30.4723
	Manga109	31.66	31.5637	-	28.6102	29.407	29.4111	-	29.1665	28.08	29.9017
SSIM \uparrow	Set5	0.9011	0.9010	0.8627	0.8432	0.8626	0.8610	0.863	0.8552	-	0.8651
	Set14	0.7917	0.7915	0.7930	0.7133	0.7476	0.7343	-	0.7353	-	0.7304
	DIV2K	-	0.8485	-	0.7720	0.7951	0.7952	0.790	0.7897	0.7932	0.7980
	BSD100	0.7455	0.7453	0.6576	0.6571	-	0.6811	0.676	0.6789	0.6869	0.6866
	Urban100	0.8153	0.8152	0.9481	0.7472	0.7673	0.7670	0.763	0.7623	0.7707	0.7764
	General100	-	0.8725	0.8537	0.8095	0.8277	0.8278	0.825	0.8262	0.8297	0.8332
	Manga109	0.9196	0.9195	-	0.8591	0.8746	0.8746	-	0.8676	0.8554	0.8786
LR-PSNR \uparrow	Set5	-	53.0951	-	46.3607	-	48.5067	-	42.4327	-	53.1781
	Set14	-	50.8098	-	43.6201	-	46.2893	-	41.5963	-	51.0679
	DIV2K	-	51.9030	-	44.8529	-	47.9757	-	42.8611	50.80	53.5488
	BSD100	-	50.3975	-	42.6756	-	45.1571	-	41.0666	49.19	51.2347
	Urban100	-	51.0009	-	42.6679	-	46.5827	-	41.6069	48.32	50.6700
	General100	-	52.6741	-	44.6786	-	48.0079	-	43.4227	50.11	52.9797
	Manga109	-	52.3321	-	44.3872	-	47.8923	-	42.8636	48.77	51.7820
LPIPS \downarrow	Set5	-	0.1691	0.0644	0.0616	0.0670	0.0637	0.061	0.0687	-	0.0603
	Set14	-	0.2718	0.1318	0.1313	0.1207	0.1309	-	0.1320	-	0.1131
	DIV2K	-	0.2526	-	0.1097	0.1011	0.1007	0.091	0.1072	0.0957	0.0956
	BSD100	-	0.3590	0.1611	0.1629	-	0.1635	0.151	0.1696	0.1500	0.1514
	Urban100	-	0.1956	0.1184	0.1186	0.1096	0.1097	0.108	0.1171	0.1065	0.1067
	General100	-	0.1668	0.0863	0.0866	0.0790	0.0794	0.077	0.0894	0.0753	0.0758
	Manga109	-	0.0977	-	0.0662	0.0553	0.0546	-	0.0688	0.0524	0.0511

**Figure 3: More visual comparisons on Urban100 [3].**

- International Conference on Computer Vision (ICCV)*. 10585–10594.
- [9] Seung Ho Park, Young Su Moon, and Nam Ik Cho. 2023. Perception-Oriented Single Image Super-Resolution using Optimal Objective Estimation. In *Proceedings of the IEEE/CVF Conference on Computer Vision and Pattern Recognition (CVPR)*. 1725–1735.
- [10] Radu Timofte, Eirikur Agustsson, Luc Van Gool, Ming-Hsuan Yang, Lei Zhang, Bee Lim, Sanghyun Son, Heewon Kim, Seungjun Nah, et al. 2017. NTIRE 2017 Challenge on Single Image Super-Resolution: Methods and Results. In *Proceedings of the IEEE/CVF Conference on Computer Vision and Pattern Recognition Workshops (CVPRW)*. 1110–1121.
- [11] Xintao Wang, Ke Yu, Chao Dong, and Chen Change Loy. 2018. Recovering Realistic Texture in Image Super-Resolution by Deep Spatial Feature Transform. In *Proceedings of the IEEE/CVF Conference on Computer Vision and Pattern Recognition (CVPR)*. 606–615.
- [12] Xintao Wang, Ke Yu, Shixiang Wu, Jinjin Gu, Yihao Liu, Chao Dong, Yu Qiao, and Chen Change Loy. 2019. ESRGAN: Enhanced Super-Resolution Generative Adversarial Networks. In *Proceedings of the European Conference on Computer Vision (ECCV)*. 63–79.

Table 4: Comparison of Ours-[a,b,c] with other artworks on 7 datasets. The best, second-best and third-best results are highlighted in bold, underline and *italic*, respectively. The symbols \uparrow and \downarrow indicate that higher or lower values of the metric are preferable.

Metric	Method	Train Datasets	Set5	Set14	DIV2K	BSD100	Urban100	General100	Manga109
PSNR \uparrow	RRDB-PSNR [12]	DF2K-OST	32.7010	28.9831	30.8888	27.8235	26.9859	31.9145	31.5637
	ESRGAN [12]	DF2K-OST	30.4618	26.2839	28.1778	25.2892	24.3617	29.4593	28.5041
	SPSR [6]	DIV2K	30.3871	26.6501	28.1824	25.4949	24.8063	29.4794	28.6102
	RRDB+LDL [4]	DIV2K	31.0007	27.2064	28.9510	26.0988	25.4781	30.1974	29.4111
	CAL-GAN [8]	DIV2K	31.0475	27.3272	28.9549	26.2581	25.2908	30.0742	29.1665
	SROOE [9]	DF2K	31.2455	27.2561	29.0990	26.1715	25.8452	30.4723	29.9017
	Ours-a	DIV2K	<u>32.3663</u>	<u>28.7621</u>	<u>30.6384</u>	<u>27.6546</u>	<u>26.5285</u>	<u>31.6047</u>	<u>30.9787</u>
	Ours-b	DIV2K	<i>32.2126</i>	<i>28.6426</i>	<i>30.4890</i>	<i>27.5176</i>	<i>26.4439</i>	<i>31.4769</i>	<i>30.8840</i>
	Ours-c	DIV2K	31.8272	28.1766	29.9858	27.0494	26.0764	31.1164	30.2763
SSIM \uparrow	RRDB-PSNR [12]	DF2K-OST	0.9010	0.7915	0.8485	0.7453	0.8152	0.8725	0.9195
	ESRGAN [12]	DF2K-OST	0.8518	0.6982	0.7761	0.6496	0.7341	0.8102	0.8604
	SPSR [6]	DIV2K	0.8432	0.7133	0.7720	0.6571	0.7472	0.8095	0.8591
	RRDB+LDL [4]	DIV2K	0.8610	0.7343	0.7952	0.6811	0.7670	0.8278	0.8746
	CAL-GAN [8]	DIV2K	0.8552	0.7353	0.7897	0.6789	0.7623	0.8262	0.8676
	SROOE [9]	DF2K	0.8651	0.7304	0.7980	0.6866	0.7764	0.8332	0.8786
	Ours-a	DIV2K	<u>0.8961</u>	<u>0.7847</u>	<u>0.8417</u>	<u>0.7379</u>	<u>0.7989</u>	<u>0.8665</u>	<u>0.9133</u>
	Ours-b	DIV2K	<i>0.8918</i>	<i>0.7800</i>	<i>0.8376</i>	<i>0.7323</i>	<i>0.7963</i>	<i>0.8629</i>	<i>0.9093</i>
	Ours-c	DIV2K	0.8804	0.7615	0.8203	0.7109	0.7812	0.8495	0.8938
LR-PSNR \uparrow	RRDB-PSNR [12]	DF2K-OST	53.0951	50.8098	51.9030	50.3975	51.0009	52.6741	52.3321
	ESRGAN [12]	DF2K-OST	46.7348	43.8433	45.9012	43.8190	42.9339	45.4220	43.9667
	SPSR [6]	DIV2K	46.3607	43.6201	44.8529	42.6756	42.6679	44.6786	44.3872
	RRDB+LDL [4]	DIV2K	48.5067	46.2893	47.9757	45.1571	46.5827	48.0079	47.8923
	CAL-GAN [8]	DIV2K	42.4327	41.5963	42.8611	41.0666	41.6069	43.4227	42.8636
	SROOE [9]	DF2K	53.1781	51.0679	53.5488	51.2347	50.6700	52.9797	51.7820
	Ours-a	DIV2K	<u>53.7806</u>	53.5768	<u>54.7418</u>	54.2712	53.7559	<u>54.1618</u>	<u>53.8049</u>
	Ours-b	DIV2K	<i>53.4204</i>	<i>53.1927</i>	<i>53.9850</i>	<i>53.3449</i>	<u>53.3426</u>	<i>53.9097</i>	53.9045
	Ours-c	DIV2K	54.3372	<u>53.3344</u>	55.2161	<u>53.3618</u>	<i>52.9401</i>	54.5283	<i>53.4195</i>
LPIPS \downarrow	RRDB-PSNR [12]	DF2K-OST	0.1691	0.2718	0.2526	0.3590	0.1956	0.1668	0.0977
	ESRGAN [12]	DF2K-OST	0.0750	0.1341	0.1155	<i>0.1617</i>	0.1228	0.0876	0.0647
	SPSR [6]	DIV2K	<i>0.0616</i>	0.1313	0.1097	0.1629	0.1186	0.0866	0.0662
	RRDB+LDL [4]	DIV2K	0.0637	<i>0.1309</i>	<i>0.1007</i>	0.1635	<u>0.1097</u>	<i>0.0794</i>	<u>0.0546</u>
	CAL-GAN [8]	DIV2K	0.0687	0.1320	0.1072	0.1696	0.1171	0.0894	0.0688
	SROOE [9]	DF2K	0.0603	0.1131	0.0956	<u>0.1514</u>	0.1067	0.0758	0.0511
	Ours-a	DIV2K	0.1293	0.2148	0.1887	0.2723	0.1811	0.1342	0.0794
	Ours-b	DIV2K	0.0849	0.1604	0.1365	0.2051	0.1432	0.0978	0.0598
	Ours-c	DIV2K	<u>0.0607</u>	<u>0.1240</u>	<u>0.0994</u>	0.1508	<i>0.1154</i>	<u>0.0776</u>	<i>0.0576</i>

[13] Zhou Wang, A.C. Bovik, H.R. Sheikh, and E.P. Simoncelli. 2004. Image Quality Assessment: from Error Visibility to Structural Similarity. *IEEE Transactions on*

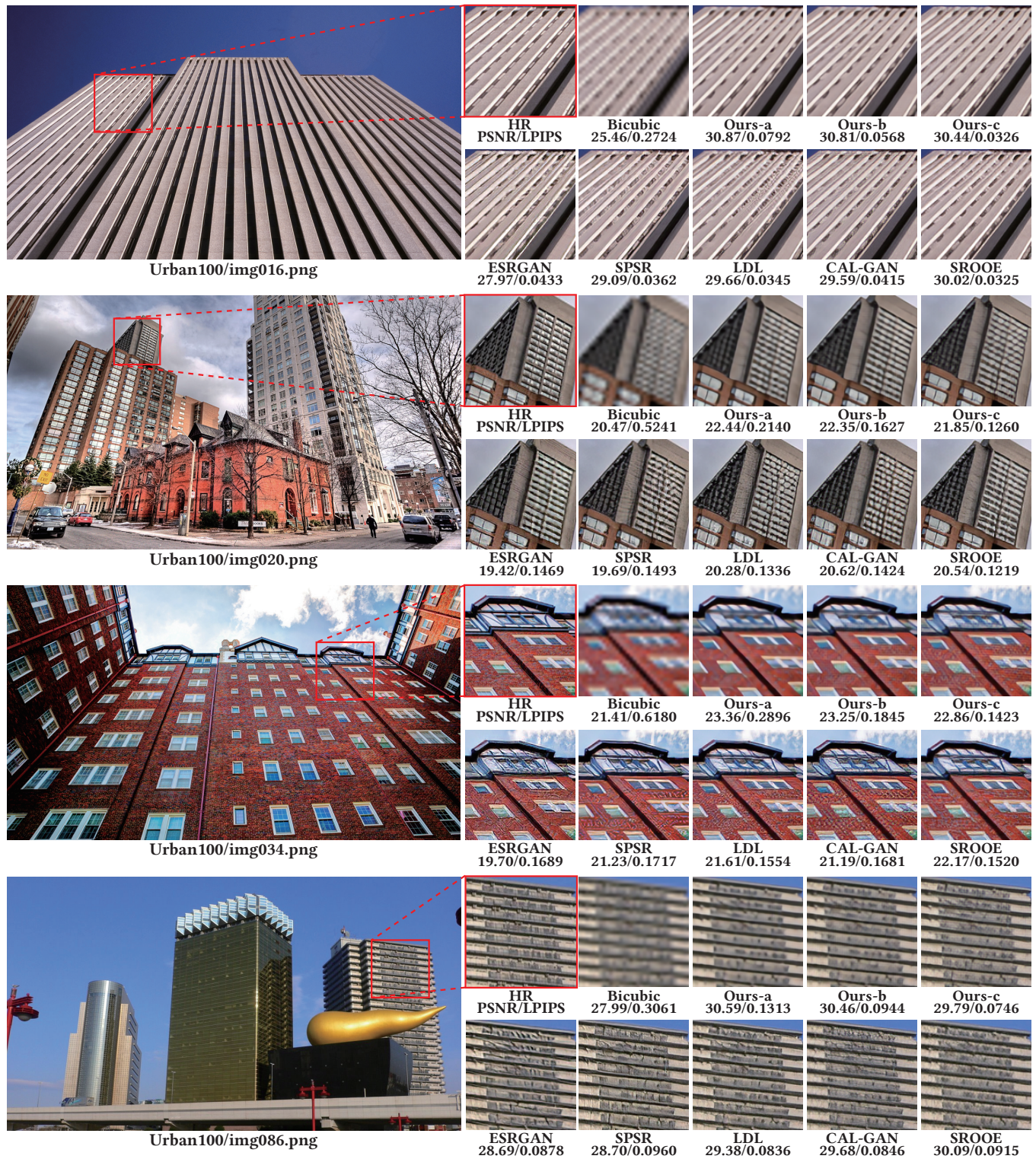


Figure 4: More visual comparisons on Urban100 [3].



Figure 5: More visual comparisons on DIV2K [1] validation set.